International Journal of Signal Processing, Image Processing and Pattern Recognition
Vol.9, No.9, (2016), pp.51-68
http://dx.doi.org/10.14257/ijsip.2016.9.9.06

Hybrid Phased-MIMO SAR: Mode Design and Performance Analysis

Lele Zhang[1] and Dianren Chen[2]

School of Electronics and Information Engineering,Changchun University of Science and Technology, Changchun 130022, China
[1]Andy_Zhang1987@126.com, [2]dianrenchen@163.com

Abstract

In this paper, we introduce an innovative scanning synthetic aperture radar (SAR) termed as the Hybrid Phased-MIMO SAR (HPMSAR) and investigate the system performance. The HPMSAR overcomes the limitations imposed by the conventional scanning SAR (ScanSAR, spotlight SAR, or Terrain Observation by Progressive Scans (TOPS) SAR) and presents the strong flexibility in imaging mode. Every subarray in HPMSAR is simultaneously pointed in the different directions and electronically steers the azimuth beam. This not only increases the illumination time per subswath entailing a high azimuth resolution but also covers an ultra-wide swath giving short-term time for global coverage. However, multidirectional scanning imaging will produce overlapped echoes and ambiguities on receive, then this paper presents the advanced processing scheme based on two-dimension (2-D) digital beamforming (DBF) with multichannel unambiguous reconstruction technology. The key of this method lies that multichannel processing technology in azimuth ensures receiving echoes free of aliasing by using a low PRF, and 2-D DBF could effectively suppress ambiguities and separate the overlapped echoes from different subswaths. Performance analysis compared with traditional methods shows output performance of interference suppression.

Keywords: *Spaceborne Hybrid Phased-MIMO SAR; Scanning SAR; 2-D DBF; Image overlap; Ambiguity*

1. Introduction

Wide unambiguous swath and high azimuth resolution will be the fundamental requirements for future SAR. The contradicting requirements between wide swath and high azimuth resolution on the design of spaceborne SAR systems have been solved by multichannel processing technology proposed in [1-2]. The transmitter and receiver in this system are always be realized on separate platforms as well as separately on the same platform and the transmit beam is fixed relative to the platform, which restricts the swath width and azimuth resolution. In the next generation of top-level spaceborne SAR system, a swath much wider than 300km is desired to shorten the revisit period with complete global coverage from a satellite, and high azimuth resolution below 1m is beneficial to obtain detailed information on specific areas. However, traditional spaceborne synthetic aperture radar (SAR) has been unable to meet the growing requirements. The scanning SAR will be the solution to achieve this goal, which could be switching among a variety of operating modes including multi-beam ScanSAR, Terrain Observation by Progressive Scans (TOPS), Spotlight and high-resolution wide-swath (HRWS) [3-6] in real time in terms of different application requirements.

At present, the scanning SAR like ScanSAR, TOPS could achieve a very wide swath by continuously switching the antenna footprint between several subswaths. In ScanSAR mode, the footprint is steered in range dimension by periodically switching the antenna

ISSN: 2005-4254 IJSIP

elevation beam to cover all subswaths subsequently [Figure 1 (b)]. In each subswath, the scan cyclically

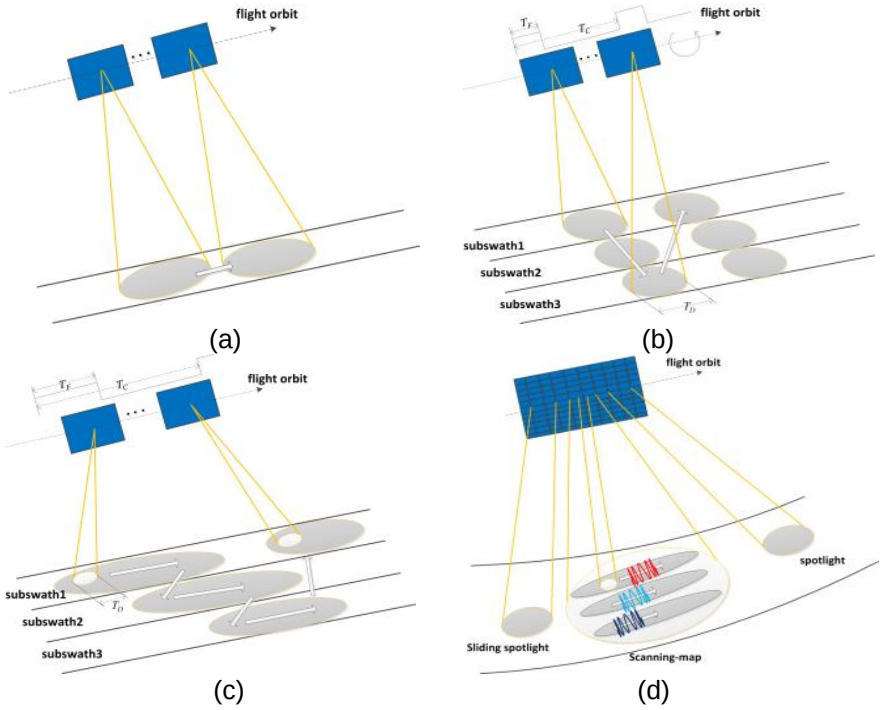

Figure 1. Multichannel SAR with Different Modes. (a) Stripmap. (b) ScanSAR. (c) TOPS. (d) HPMSAR

acquires bursts for a dwell time T_D repeated with a period T_C, and the burst duration time is T_F. TOPSAR [Figure 1 (c)] is a recently proposed acquisition mode to achieve the same wide swath imaging as in ScanSAR, but obviously reducing its drawbacks [7]. This more sophisticated burst mode is not only electronically steering the azimuth antenna pattern from back to forth, but also switching in range. Unfortunately, the azimuth resolution in both ScanSAR and TOPSAR (compared with the STRIPMAP mode [Figure 1 (a)]) is reduced obviously by a shorter target illumination time, entailing a coarsened azimuth resolution, thus excluding the capability of high-resolution imaging.

In conclusion, advanced concepts are needed for the imaging of an ultrawide swath of several hundred kilometers with high azimuth resolution well below 1 m. In recent years, Hybrid MIMO Phased Array Radar (HMPAR) [8-12] was theoretically proposed and researched. The HMPAR is to partition the transmitting array into multi-array which is allowed to overlap, and each of these subarrays is in turn used to emit the orthogonal signal through transmitting beamforming towards arbitrary direction in space. Although the real price of spaceborne HMPAR and radar data generated with the available instrument technology of today is too high, affordable operational instruments will play a key role in the very near future. In [13], we further investigated a combination between HMPAR and SAR, presented the digital beamforming on receive in elevation for spaceborne Hybrid Phased-MIMO SAR. At present, the scanning-SAR, utilizing digital beamforming on receive, is increasingly being considered for future missions. Here we term this system as HPMSAR [Figure 1 (d)]. HPMSAR may be the best choice for future scanning-radar imaging system. We are very well aware of the advantages of MIMO with multidimensional waveform encoding [14-16], and phased array radar respectively. Every subswath corresponds to different orthogonal waveforms as shown in Figure 1 (d) and this will improve system performance obviously [17]. HPMSAR can achieve two-dimension

scanning at the same time that every subarray in HPMSAR is simultaneously pointed in the different directions and electronically steers the azimuth beam. This not only increases the illumination time per subswath entailing a high azimuth resolution but also covers an ultra-wide swath giving short-term time series of images. However, in such a system, overlapped echoes and ambiguities are always produced, and thus, signal reconstruction is necessary for SAR imaging.

In this paper a novel multichannel processing technology was proposed, which is a combination between 2-D advanced DBF and multichannel unambiguous reconstruction technology for HPMSAR. A detailed investigation of this processing technology will be given in this paper.

This paper is organized as follows. Section 2 reviews HPMSAR system design including HPMSAR principle overview, performance parameter definition, azimuth resolution analysis, transmit beampattern design, TFD support and PRF selection. Then, Section 3 turns the focus to 2-D DBF with multi-aperture reconstruction algorithm. Finally, concluding summaries are drawn in Section 4.

2. HPMSAR SYSTEM DESIGN

2.1. HPMSAR Principle Overview

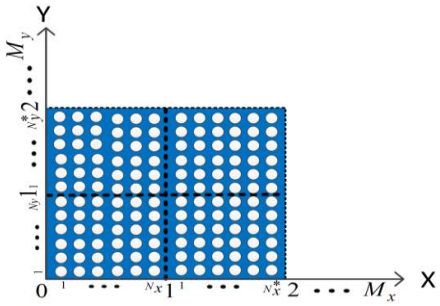

Figure 2. HPMSAR Notional Concept

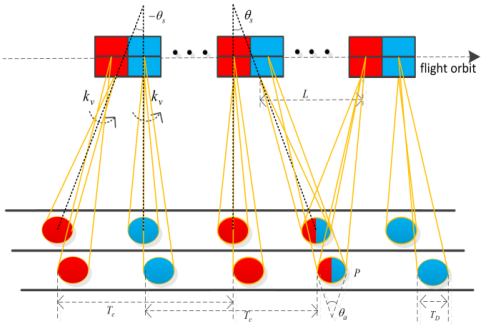

Figure 3. HPMSAR in Continuation-Mode

In HPMSAR, there is a rectangular array that can be referred to as a MN array, organized into M subarrays of N elements each, as shown in Figure 2. In this coordinate axis, two-dimension configurations have much more probability.There are $M = M_x M_y$, $N = N_x N_y$, N_x may be not equal to N_x^* , which will be setting separately for different applications, so that the transmit beampatterns will afford the greatest flexibility. We will often use the case $M = N$ because of its most flexibility in transmit beampattern design. Every subarray will produce a beampattern that illuminates the fraction $1/M$ of the total search volume, and if the beams are forming appropriately, transmit energy will be distributed evenly for the entire search volume. When all M signals are perfectly correlative, and all M subarrays are pointed in the same direction, then this planar array acts as one large phased array.

As we know, STRIPMAP and spotlight SAR have excellent azimuth resolution $\delta_{az} \le 1$ m, but the swath width is greatly reduced. This will increase many acquisitions and need a long repetition time for global earth. While the ScanSAR and TOPS can reach more than 300km of the swath, but the increased swath coverage is achieved by the tradeoff with a reduced azimuth resolution. This results in a reduced azimuth resolution due to the reduction in the dwell time T_D of the antenna footprint on every target within the swath. HPMSAR could achieve

electronically 2-D scanning in different subswaths by switching different subarrays, which could operate in continuation-mode that is multidirectional continuous scanning in azimuth, as shown in Figure 3. This does not correspond to any current one, but it could be an interesting proposal for the future. The whole scanning angle in terms of the number of subarrays in azimuth is divided into θ_s .

$$\theta_s = \theta_a / M_x \tag{1}$$

When the number of subarrays in azimuth is infinite, it can be understood as a stripmap SAR with a large beamwidth, which could achieve ultimate azimuth resolution. But this is unreasonable and impossible greatly. We set two subarrays with different colors in azimuth, the red one and blue one scan simultaneously with the same cycle T_c that defines the time for the whole scanning range $(-\theta_s, \theta_s)$. The scanning angle are $(-\theta_s, 0)$ and $(\theta_s, 0)$ respectively for every subarray in azimuth. This greatly reduces the scanning cycle and keeps the original scanning rate. Consequently, total azimuth signal bandwidth might span over several Pulse Repetition Frequency (PRF) intervals. The change in the central frequency is the unavoidable consequence of the one-to-one time–frequency mapping peculiar of the synthetic aperture, as the spectrum of a target at slow time τ would be centered on an azimuth-varying Doppler

$$f_0(\tau) = k_d \tau \tag{2}$$

The bandwidth for each target would be

$$B_b = |k_d| T_D \tag{3}$$

where k_d is the Doppler rate. In the simplified rectilinear geometry, we can approximate as follows

$$k_d = \frac{1}{2\pi} \frac{\partial^2 R(\tau)}{\partial \tau^2} = -\frac{2v_s^2}{\lambda R_{0,i}} \tag{4}$$

$R_{0,i}$ is the closest approach distance, the index i accounts for the varying beam velocity and mean slant range of the respective subswath, λ is the wavelength, and v_s is the sensor velocity. Considering the geometry in Figure 3, we assume the antenna beam to rotate at a negative rate k_v (rad/s), so that it points in the direction

$$\varphi_d = k_v \tau \tag{5}$$

and a cycle time T_c can be derived by

$$T_c = |\theta_s / k_v| \tag{6}$$

Doppler bandwidth acquired for each target in the swath is no longer directly related only to the dwell time T_D but also to the rate k_v . In order to achieve a required azimuth resolution δ_{az} , the effective illumination time T_a is given by the following equation

$$T_a = \rho T_D \tag{7}$$

ρ is a constant coefficient and given by

$$\rho \approx T_R / T_c \text{ , with } \rho \geq 1 \tag{8}$$

where T_R is whole target illumination time ranging from the first illumination moment to final illumination moment, T_D is target dwell time in once scanning cycle and can be expressed as

$$T_D = \frac{\lambda R_{0,i} B_b}{2 v_s v_{g,i}} \approx \frac{\lambda R_{0,i} 0.89}{2 v_s \delta_{az}} \tag{9}$$

where $v_{g,i}$ is beam velocity and it can be neglected in the following.

2.2. HPMSAR Performance Parameter Definition

This section provides a definition of the quantities involved in the evaluation of the HPMSAR system performance. When PRF is set too high, the radar return from two successive pulses will be overlapped at the receiver and this type of ambiguity is referred to as range ambiguity [18]. Multiple-swath imaging in range will result in a large number of echoes and overlapped echoes from different swaths must be produced. All this is evaluated by the Range-Ambiguity-to-Signal Ratio (RASR) performance and its definition as a function of slant range R_i is given by [19]

$$RASR_i = \frac{R_i^3 \sin(\theta_{0,i})}{\sigma_{0,i} \left| G_{el}(\theta) \right|^2} \sum_{\substack{l \neq 0 \\ l=-M_N}}^{M_F} \frac{\sigma_{l,i} \left| G_{el}(\theta_l) \right|^2}{R_{l,i}^3 \sin(\theta_{l,i})} \tag{10}$$

where $G_{el}(\theta)$ represents the receive antenna pattern in elevation that will be given in Section 2.3, and the range ambiguity suppression is mainly achieved by the narrow Scan-On-Receive (SCORE) receive beam, rather than by the transmit beam; θ is the beam steering angle; M_F , M_N are the number of ambiguities considered in the calculation in near range and far range, respectively. $\sigma_{l,i}$, $\sigma_{0,i}$ are the corresponding normalized backscatter coefficient. $\sigma_{0,i}$ and $\theta_{0,i}$ are the corresponding parameters of the desired unambiguous return. The subscript l denotes the corresponding quantities associated to the ambiguous signals.

In fact, the Doppler spectrum is not strictly band limited due to the sidelobes of the azimuth antenna pattern. As a consequence, Doppler frequency components outside the sampling interval $-PRF/2 \le f_{sig} \le +PRF/2$ are folded back into the processed Doppler frequency range, producing ambiguities. In addition, when the pointing angle is steered away from boresight, grating lobe gain increases and the main lobe gain decreases, most of the grating lobes energy is also folded back into the processed bandwidth. This is the worst case causing a drop of performances, so we must consider it. Azimuth-Ambiguity-to-Signal Ratio (AASR) is defined as

$$AASR_i = \frac{\sum_{m \neq 0, m=-N_a}^{N_a} \sigma_{m,i} \int_{-B_b/2}^{B_b/2} \left| G_{2way,az}(f_D + mPRF) \right|^2 df_D + P_g}{\sigma_{0,i} \int_{-B_b/2}^{B_b/2} \left| G_{2way,az}(f_D) \right|^2 df_D} \tag{11}$$

where f_D is the Doppler frequency; B_b is the processed azimuth bandwidth; $G_{az}(f_D)$ is the two-way (transmit/receive) azimuth antenna pattern as a function of the Doppler frequency; N_a is the number of ambiguities considered in the calculation. $\sigma_{m,i}$, $\sigma_{0,i}$ are the corresponding normalized backscatter coefficient. P_g is the total ambiguity power caused by grating lobes.

2.3. Azimuth Resolution

In TOPS, each target will be illuminated by the steered antenna for a ground footprint, which is equivalent to that of a fixed antenna, but shrunk by a factor

$$\delta_{az}^{TOPS} = \alpha \delta_{az}^{STRIP} \tag{12}$$

Where

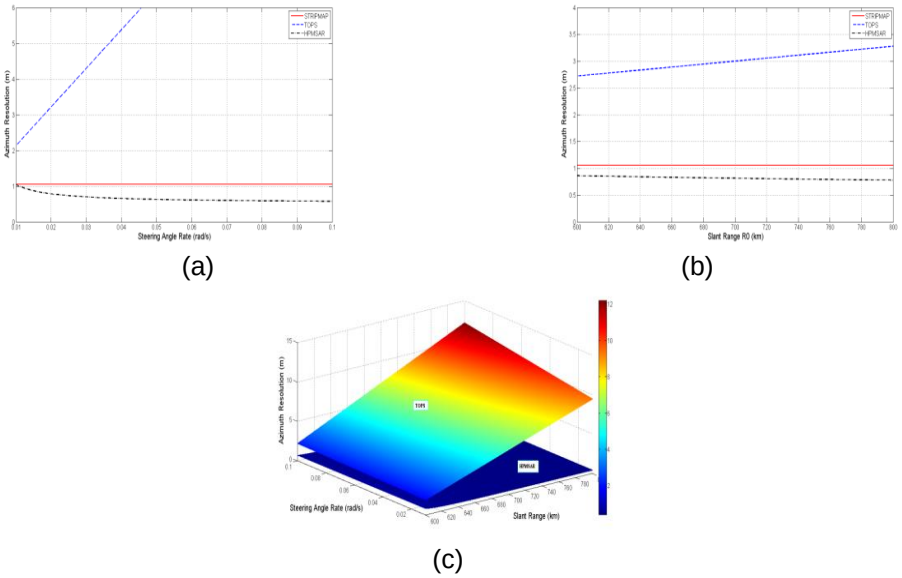

(a) (b)

(c)

Figure 4. Geometric Azimuth Resolution Comparison of STRIPMAP, TOPS and HPMSAR. (a) Azimuth Resolution Versus Steering Angle Rate. (b) Azimuth Resolution Versus Slant Range R_0. (c) Azimuth Resolution Versus Slant Range R_0 and Steering Angle Rate k_v

$$\alpha = 1 + \frac{R_0 k_v^{TOPS}}{v_s} \quad 1 \tag{13}$$

$$\delta_{az}^{STRIP} \approx \frac{v_s}{|k_d| T_D} = \frac{\lambda}{2\theta_{BW}} \tag{14}$$

θ_{BW} is angular range for the generic target illumination in STRIPMAP SAR system, the choice of θ_{BW} is a tradeoff between the desire for good resolution (demanding large angular intervals) and the need for strong ambiguities suppression, which requires processing small angular apertures. In order to increase the synthetic angular range θ_a of the generic target in HPMSAR, we used two ways:

1) Design the rectangular transmit beampattern through weighting in transmit side.
2) Continuous scanning with two subarrays in azimuth proposed in Section 2.1

In HPMSAR, the illumination time T_a is increased by ρ times showing in Equation (7) so the azimuth resolution δ_{az}^{HPMSAR} can be defined as

$$\begin{aligned}\delta_{az}^{HPMSAR} &= \left(\alpha/\rho\right)\delta_{az}^{STRIP} \\ &= \frac{\left(v_s + R_{0,i}k_{v,i}\right)\theta_s}{Lk_{v,i}}\delta_{az}^{STRIP}\end{aligned} \tag{15}$$

where $L \approx R_{0,i}\theta_a$, and Equation 13 can be rewritten as

$$\begin{aligned}\delta_{az}^{HPMSAR} &= \left(\alpha/\rho\right)\delta_{az}^{STRIP} \\ &= \frac{\left(v_s + R_{0,i}k_{v,i}\right)\theta_s}{Lk_{v,i}}\delta_{az}^{STRIP} \\ &= \frac{\left(v_s + R_{0,i}k_{v,i}\right)\theta_s}{R_{0,i}\theta_a k_{v,i}}\delta_{az}^{STRIP} \\ &= \left(\frac{\theta_s}{\theta_a} + \frac{v_s\theta_s}{R_{0,i}k_{v,i}\theta_a}\right)\delta_{az}^{STRIP} \\ &= \beta\delta_{az}^{STRIP}\end{aligned} \tag{16}$$

and $\beta = \theta_s/\theta_a\left(1+v_s/R_{0,i}k_{v,i}\right)$ 1, $\theta_s/\theta_a \le 1/2$, in other words, this situation is much more better than a STRIPMAP SAR with the improved azimuth resolution as shown in Figure 4, where azimuth resolution in HPMSAR is approximately 0.5m under the condition of $\theta_s/\theta_a = 1/2$. This is not the best case in our system, the better resolution than this is much possible. Hence, since we want equal resolution on all the subswaths, we obtain

$$k_{v,i} = \frac{\lambda\theta_s v_s}{\left(2\delta_{az}^{HPMSAR}\theta_a\theta_{BW} - \lambda\theta_s\right)R_{0,i}},\ \theta_a > \theta_s \ge \theta_{BW} \tag{17}$$

So HPMSAR could achieve the same swath width as in TOPS and ScanSAR, and its azimuth resolution has been improved much more. The bandwidth of a target is

$$B_P = \frac{2v_s}{\lambda}\sin\left(\theta_a\right) \tag{18}$$

Good azimuth resolution δ^{HPMSAR} requires a wide Doppler bandwidth B_P, and the wide B_P needs a high pulse repetition frequency (PRF) to sample it according to the Nyquist criterion. In contrast, to unambiguously image a wide swath on ground, a large interval between subsequent pulses (a low PRF) is favorable. The relationship between azimuth resolution δ^{HPMSAR} and width of range swath on ground (W_g) can be expressed as

$$W_g/\delta^{HPMSAR} < c/\left(2v_s\sin\left(\theta_i\right)\right) \tag{19}$$

and

$$W_g \approx \left(1/PRF - T_p\right)c_0/2\sin\left(\theta_i\right) \tag{20}$$

where θ_i is the incident angle. This problem between azimuth resolution and swath width can be solved by multi-channel receiving technology [1] and we will describe it in Section 3.

2.4. Transmit Beampattern Design

HPMSAR combines the merits of phased-array radar and MIMO radar. So the resulting transmit beampattern of each subarray in HPMSAR is approximately rectangular [10]. This could be advantageous for tracking radars operating on rapidly maneuvering or uncertain targets that could move outside the phased-array pencil beam. The beamwidth α in electrical angle space is varied from 0 to 1 and its unit is rad. For $\alpha = 0$, HPMSAR is MIMO radar with omnidirectional beampattern in red color, when $\alpha = 1$, HPMSAR acts as one phased array in black color as shown in Figure 5 (b). An ideal normalized directivity gain is assumed for each element:

$$G_0(\varphi) = \text{sinc}^2\left(\frac{L_0}{\lambda}\sin(\varphi)\right) \tag{21}$$

where L_0 represents the length of the single element; φ represents the squint angle in azimuth and the off-boresight angle in elevation. Consider a HPMSAR system with the case of a uniform linear array and the transmit beampattern can be expressed as

$$G_T(\varphi,\tau) = G_0(\varphi)\left|\frac{1}{N}\sum_{\substack{l\neq 0 \\ l=-N_x}}^{N_x}\left(N_x - |l|\right)C_l(\varphi)e^{j\left(2\pi dl/\lambda\right)\sin(\psi(\tau))}\right|^2 \tag{22}$$

where $C_l(\varphi)$ is the excitation coefficients and given by

$$C_l(\varphi) = \mathrm{a}_l\left(\frac{\sin(\alpha\pi l)}{\sin(\alpha\pi l/P)}\right)e^{-j\left(2\pi dl/\lambda\right)\sin(\varphi)} \tag{23}$$

d is the array spacing, $N = 2N_x$ is the number of transmitters, P is the length of the transmitted codes each having unit energy, $\psi(\tau)$ has been defined in Equation (5), a_l is excitation coefficients amplitude, then the transmitted signals can be represented as

$$\tilde{\boldsymbol{s}}(n) = \left[\tilde{s}_1(n) \quad \tilde{s}_2(n) \quad \ldots \quad \tilde{s}_{N-1}(n)\right]^T \tag{24}$$

Hence the matrix form of the transmitted waveforms of the k th subarray is

$$\boldsymbol{s}_k = \left[\tilde{\boldsymbol{s}}(0) \quad \tilde{\boldsymbol{s}}(1) \quad \ldots \quad \tilde{\boldsymbol{s}}(P-1)\right] \tag{25}$$

and the transmitted signal of HPMSAR is

$$\boldsymbol{S} = \left[\boldsymbol{s}_1 \quad \ldots \quad \boldsymbol{s}_M\right] \tag{26}$$

Figure 5 (a), depicts the rectangular transmit beampattern with 100-element array at half-wavelength spacing and $\alpha = 0.05$,from the simulation, there is a -50dB uniform sidelobe level approximately and this will be varied with the change of N and α , here we will not expand it and this is not the key point for this paper. Note the desirable rectangular beampattern made possible in this case by the large value of N .

This methodology can be extended to rectangular arrays. Suppose that the transmitters of each subarray are arranged in a M_x by M_y uniformly spaced grid, where $M_x \times M_y = M$. They are particularly useful for the proposed HPMSAR architecture, since the every subarray could easily be chosen as a rectangular array.

The subarrays can be steered in different directions and a fixed array of MN transmitters can be reconfigured into rectangular subarrays in a number of different ways and signal covariance matrix can then be expressed as

$$\boldsymbol{R}_h = \boldsymbol{S}_h \boldsymbol{S}_h^H \tag{27}$$

$$\boldsymbol{R}_v = \boldsymbol{S}_v \boldsymbol{S}_v^H \tag{28}$$

where $(\cdot)^H$ stands for the Hermitian transpose, $\boldsymbol{R}_h$ and $\boldsymbol{R}_v$ are the signal correlation matrices for $\boldsymbol{S}_h$ signals and the $\boldsymbol{S}_v$ signals, respectively, and the subscripts h and v connote "horizontal" and "vertical," respectively. If every beam formed by each of M subarrays is pointed in the different directions, the steering vector of every subarray in horizontal and vertical are

$$\boldsymbol{a}_k(\theta_k) = \left[1 \quad e^{-j(2\pi f_0 d \sin\theta_k / c)} \quad \ldots \quad e^{-j(2\pi f_0 (N_x - 1) d \sin\theta_k / c)}\right]^T \tag{29}$$

$$\boldsymbol{b}_k(\theta_k) = \left[1 \quad e^{-j(2\pi f_0 d \sin\theta_k / c)} \quad \ldots \quad e^{-j(2\pi f_0 (N_y - 1) d \sin\theta_k / c)}\right]^T \tag{30}$$

The steering vector matrices of HPMSAR in horizontal and vertical are

$$\boldsymbol{A}(\theta) = \left[\boldsymbol{a}_1(\theta_1) \quad \ldots \quad \boldsymbol{a}_{M_X}(\theta_M)\right] \tag{31}$$

$$\boldsymbol{B}(\theta) = \left[\boldsymbol{b}_1(\theta_1) \quad \ldots \quad \boldsymbol{b}_{M_y}(\theta_M)\right] \tag{32}$$

and the synthesis steering vector matrix of HPMSAR is

$$\boldsymbol{U} = \boldsymbol{A}(\theta) \otimes \boldsymbol{B}(\theta) \tag{33}$$

where $\otimes$ is the Kronecker product operator, for a uniform rectangular array it is convenient to express the array response vector as a function of two electrical angles u and v. We describe the coordinate system in $x-y$ plane with θ and φ representing azimuth and elevation, respectively, then

$$\begin{cases} u = \sin(\theta) \\ v = \sin(\varphi) \end{cases} \tag{34}$$

So the rectangular beampattern of each subarray for HPMSAR is

$$\begin{aligned} \boldsymbol{G}_k(u,v) &= \left(\boldsymbol{a}_k(u) \otimes \boldsymbol{b}_k(v)\right)^T \left(\boldsymbol{R}_h \otimes \boldsymbol{R}_v\right) \left(\boldsymbol{a}_k(u) \otimes b_k(v)\right)^* \\ &= \left(\boldsymbol{a}_k{}^T(u) \boldsymbol{R}_h \boldsymbol{a}_k{}^*(u)\right) \otimes \left(\boldsymbol{b}_k{}^T(v) \boldsymbol{R}_v \boldsymbol{b}_k{}^*(v)\right) \end{aligned} \tag{35}$$

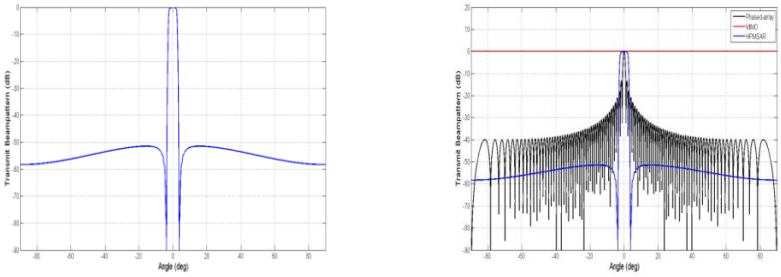

(a) (b)

Figure 5. HPMSAR Beampattern for a Uniform Linear Array. (a) Single Rectangular Beampattern. (b) Comparison of MIMO, Phased-Array and HPMSAR

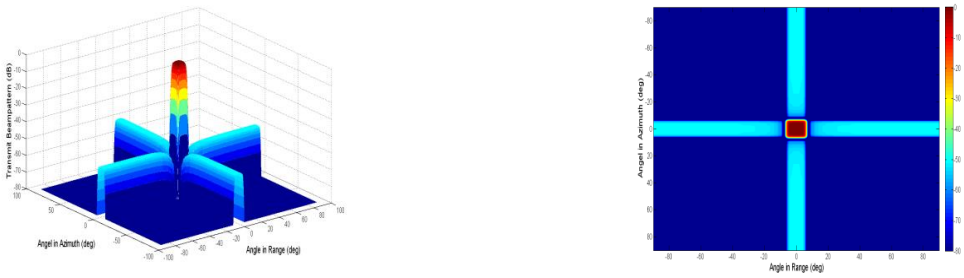

(a) (b)

Figure 6. HPMSAR Beampattern for a Rectangular Array

Figure 6, illustrates a three-dimensional view of HPMSAR beampattern. This pattern is shown on a linear scale from -80dB to 0dB, using the MATLAB "jet" colormap and the simulation parameter is same as Figure 5.

2.5. TFD Support

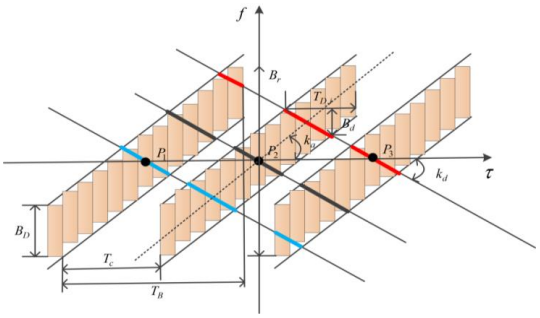

Figure 7. TFD Support for HPMSAR

The raw data support in the slow time/frequency domain (TFD) is outlined in Figure 7, for the proposed HPMSAR. In the figure, three targets $P_1 - P_3$ are represented in their zero-Doppler time, whereas their Doppler histories are shown by thin lines with negative slopes, equal to the Doppler rate k_d. The TFD support is represented by the light yellow shaded blocks: the shading recalls the AAP weighting. The antenna pointing sweeps with time $T_B \approx 2T_c$. In practice, every target in Figure 7 would be observed during several cycles with the different colors, albeit at different Doppler, for the complete dwell time and Doppler bandwidth are as follows

$$T_a = \sum_{i=1}^{\rho} T_{D,i} \tag{36}$$

$$B_a = k_a T_a \quad N \cdot PRF \tag{37}$$

and k_a is a Doppler centroid rate and expressed as

$$k_a \approx -\frac{2v_s}{\lambda} k_v \tag{38}$$

2.6. PRF Selection

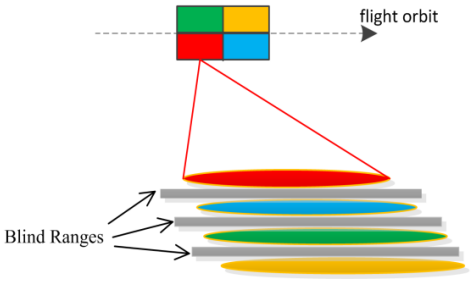

Figure 8. Blind Ranges for a Given PRF

A drawback of the continuation-mode in HPMSAR is the blind ranges that are due to the fact that each subarray cannot receive while it is transmitting, and the "blind ranges" is always presented between adjacent subswaths as shown in Figure 8. The four subarrays corresponding to different colors are forming the subbeams towards different swaths. This can be overcome in a bistatic SAR where the transmitter is sufficiently separated from the receiver. In HPMSAR system, we could use parts of the receiving antenna for transmit to solve this problem. However, a combined transmit–receive antenna together is the main trends of development in future. To avoid a separate transmit satellite, one can employ a variation of the PRF in HPMSAR which shifts the blind ranges across the swath [20-21]. The PRF variation could either be implemented in discrete steps leading to a multiple beam mode or a pulse-to-pulse variation of the PRI. This concept allows the imaging of a wide continuous swath and provides better performance but requires a dedicated SAR processing which is currently under development.

We will use the processing technology that combines 2-D DBF with multichannel processing technology in Section 3, which will make a good choice for PRF selection and this value could be very low to avoid spectrum aliasing.

3. Two-Dimension DBF with Multichannel Azimuth Processing

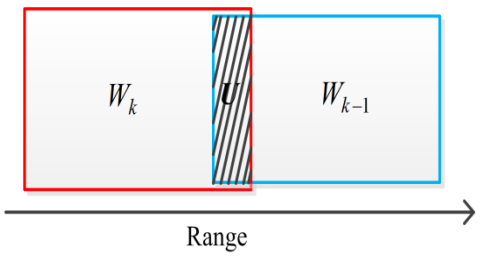

Figure 9. Overlapped Area in Range

The HPMSAR system will also meet the same problem with conventional scanning SAR:

(1) The ambiguities in azimuth and range that are caused by the PRF selection and the sidelobes of transmit beampattern in azimuth respectively. This has been discussed in Section 2.2. When the pointing angle is steered away from boresight, grating lobes arise. The echoes corresponding to the grating lobes are also ambiguities. So these will influence the image quality.

(2) Overlapped areas are shown in Figure 9, where U is the overlapped area, W_k and W_{k-1} are the subswaths. This is just an abridged general view without serious range ambiguity. Because of the multidirectional continuous scanning in azimuth, it will produce a large number of overlapped echoes from different subswaths in the range time domain especially the adjacent area between two subswaths, and this will result in terrible image.

Table 1. System Parameters Used in the Simulation

PARAMETER	VALUE	PARAMETER	VALUE
Orbit Height	576km	Elevation Beamwidth	9°
Sub-swath	2	Azimuth Beamwidth	0.33°
Bandwidth	100MHz	Subpulse Duration	50μs
Carrier Frequency	9.65GHz	Number of Subapertures in Azimuth	20
Satellite velocity	7608m/s	Number of Subapertures in Elevation	100

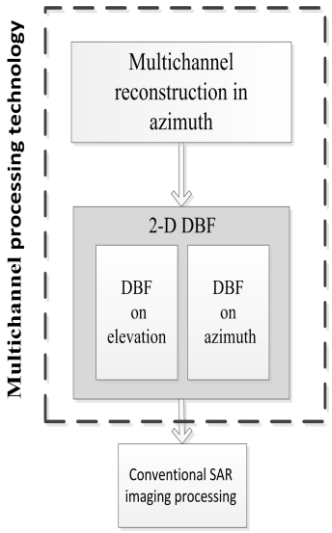

Figure 10. Block Diagram of the Processing Scheme for HPMSAR

We will combine our advanced 2-D beamforming approach with Multi-Aperture Reconstruction Algorithm to cope with these problems. Figure 10 shows the processing chain for HPMSAR, where the dashed square is utilized to denote preprocessing part in the entire processing scheme. Such block shows flexibility with respect to the receiving pattern and the effective sampling ratio given by the number of different reconstructed channels in azimuth.

The multi-aperture reconstruction algorithm is founded on a generalization of the sampling theorem according to which N independent representations of a signal, each subsampled at $1/N$ th of the signal's Nyquist frequency, allow for the unambiguous "reconstruction" of the original signal from the aliased Doppler spectra of the N representations. The essential idea of these techniques is to substitute high sampling frequency in space domain for high sampling frequency in the time domain by means of multiple receiver channels. Each of the N receiver channels' signal is mixed, digitized, and stored. In azimuth dimension, this enables a coherent combination of the N subsampled and hence aliased signals to a single output signal that is sampled with $N \cdot PRF$ and free of aliasing [22]. Here we will not represent this algorithm and mainly focus on our 2-D beamforming.

Consider a system according to Figure 11, with exemplary $N = 2$ apertures, the original system with single aperture and $PRF = B_a/2$. The simulation result is obvious that the two ambiguities caused by under sampling in the original system are removed in a two-channel system

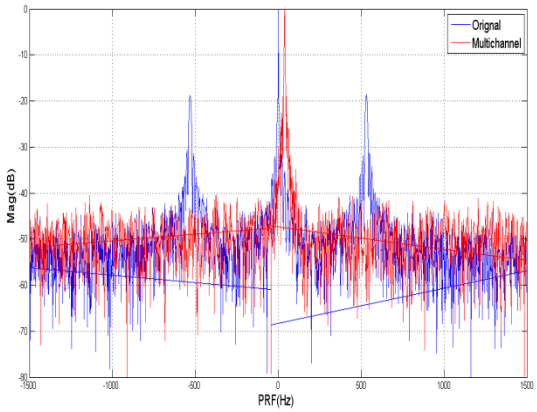

Figure 11. Reconstruction for Multichannel System

3.1. DBF in Elevation

This system uses DBF on receive to steer in real time a narrow beam toward the direction of arrival of the radar echo from these subswaths, exploiting the one-to-one relationship between the radar subpulses travel time and its direction of arrival (this is also referred to as scan on receive (SCORE).

A linearly constrained beamformer can be formulated as that of finding the weight vector $\boldsymbol{W}$ which minimizes the output power

$$\min_{\boldsymbol{W}} \boldsymbol{W}^H \boldsymbol{R}_{XX} \boldsymbol{W} \quad \text{s.t.} \quad \boldsymbol{C}^H \boldsymbol{W} = \boldsymbol{f} \tag{39}$$

where $\boldsymbol{R}_{XX}$ is the interference-plus-noise covariance matrix, $\boldsymbol{C}$ is the constraint matrix, the vector $\boldsymbol{f}$ specifies the corresponding constraint value for each vector.

It is well known that the optimal solution of the minimization problem defined above is

$$\boldsymbol{W}_{el} = \boldsymbol{R}_{XX}^{-1} \boldsymbol{C} \left(\boldsymbol{C}^H \boldsymbol{R}_{XX}^{-1} \boldsymbol{C} \right)^{-1} \boldsymbol{f} \tag{40}$$

and then we will design $\boldsymbol{C}$, $\boldsymbol{f}$ and $\boldsymbol{R}_{XX}^{-1}$ appropriately. Where $\boldsymbol{C}$ includes three parts and their analytical expressions have the form

$$\boldsymbol{C} = \left[\overline{\boldsymbol{W}_0} \quad \overline{\boldsymbol{C}_0} \quad \boldsymbol{A}(\theta_m) \right] \tag{41}$$

and

$$\boldsymbol{f} = \left[1 \quad 0 \quad \cdots \quad 0 \right]^T \tag{42}$$

$$\overline{\boldsymbol{W}_0} = \frac{\boldsymbol{W}_0}{\boldsymbol{W}_0^H \boldsymbol{W}_0} \tag{43}$$

where $\boldsymbol{W}_0$ denotes the weighting coefficients of the desired quiescent response, $\overline{\boldsymbol{C}_0}$ is to prevent the desired signal from being cancelled by adaptive weights and the specific expression shows in the literature [23], $\boldsymbol{A}(\theta_m)$ is the steering vector matrix of interference signal. We want to achieve desired quiescent response with an overall low sidelobe and B nulls at the jammer direction.

Suppose that there are N elements for reception and the covariance inverse matrix is expressed in the terms of feature space theory as follows

$$\begin{aligned} \boldsymbol{R}_{XX}^{-1} &= \sum_{i=1}^{B} \lambda_i^{-1} e_i e_i^H + \sum_{i=B+1}^{N} \sigma_n^{-2} e_i e_i^H \\ &= \sigma_n^{-2} \left[\boldsymbol{I} - \sum_{i=1}^{N} \frac{\lambda_i - \sigma_n^2}{\lambda_i} e_i e_i^H \right] \end{aligned} \tag{44}$$

where e_i is the eigenvector of the $\boldsymbol{R}_{XX}$, λ_i corresponds to its eigenvalue. In order to achieve the desired adaptive low sidelobe and reduce the small eigenvalue interference for its eigenvector, we apply the technique of diagonal loading in [24] that add the appropriate value Q to every eigenvalue. So the expression can be rewritten as

$$\boldsymbol{W}_{el} = \left[\boldsymbol{I} - \sum_{i=1}^{N} \frac{\lambda_i + Q - \sigma_n^2}{\lambda_i + Q} e_i e_i^H \right] \boldsymbol{C} \left(\boldsymbol{C}^H \left[\boldsymbol{I} - \sum_{i=1}^{N} \frac{\lambda_i + Q - \sigma_n^2}{\lambda_i + Q} e_i e_i^H \right] \boldsymbol{C} \right)^{-1} \boldsymbol{f} \tag{45}$$

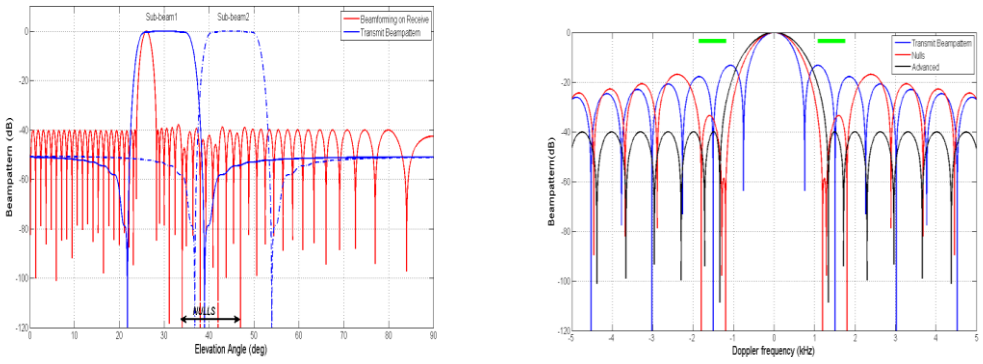

(a) (b)

Figure 12. Transmit (Blue Color Line) and Receive Patterns (Red Line) of the HPMSAR System. (a) Elevation Patterns. (b) Azimuth Patterns.

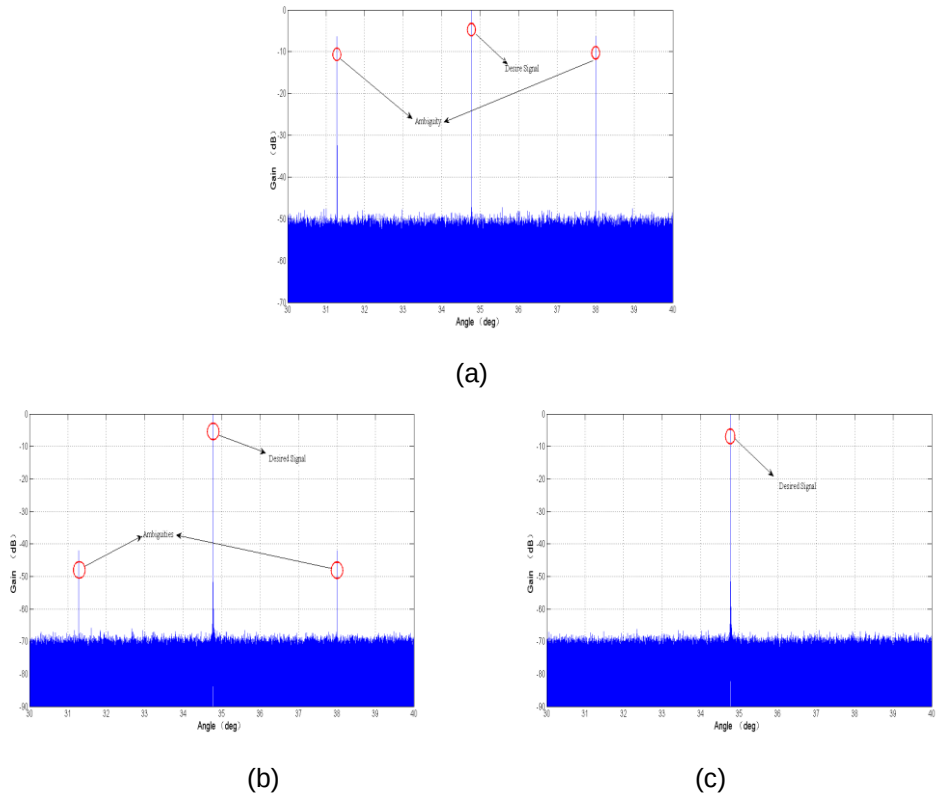

Figure 13. Range Compression for Three Point Targets. (a) Raw Data without Beamforming. (b) Beamforming without Setting Nulls. (c) Advanced Beamforming

In fact, the useful echo is always, that is, for each point on the swath, weighted by the maximum of the receive pattern, whereas the ambiguous echoes are strongly attenuated by the receive pattern sidelobes as shown in Figure 12 (a). Figure 13, shows three range compression results, where ambiguities presents high receiving gain in Figure 13(a), and this will result in terrible image. Figure 13 (b) describes the beamforming with desired receiving pattern and without setting nulls that ambiguities are suppressed below -40dB. Figure 13 (c), are the advanced beamforming that the ambiguities are removed. This result in the good range-ambiguity-suppression for different subswaths in Figure 14(a), of better than −55 dB compared with the conventional method without this DBF.

3.2. DBF in Azimuth

This space-time approach is based on adaptively adjusting the weighting coefficients of the azimuth channels to steer the nulls in the resulting joint antenna pattern to the angles corresponding to the ambiguous Doppler frequencies. This corresponds to a spatial filtering of the data to suppress ambiguous frequencies in the azimuth signal. The coherent combination of all signals in a dedicated multichannel processor enables the generation of a HRWS image.

Figure 12 (b), shows the beamforming in azimuth, the red color line represent beampattern with nulls, which are below -30dB, at the first and second sidelobe marked with the green bars. The black one is the advanced method that is same as (46) with low sidelobes and the ambiguity performance of the HPMSAR system is shown in Figure 14(b), versus the PRF on the swath. The red one is constant value -

20dB for every subswath and the blue one is below −35dB. Its value is depends on the PRF, the antenna length, and the processed azimuth bandwidth.

So the system weighting of HPMSAR is given by

$$\boldsymbol{W}_{system} = \boldsymbol{W}_{el} \otimes \boldsymbol{W}_{az} \tag{49}$$

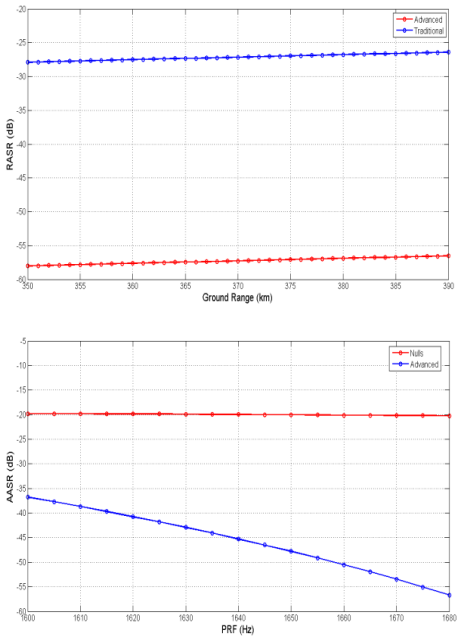

(a) (b)

Figure 14. Performance Analysis of the HPMSAR System. (a) RASR. (b) AASR

4. Conclusion

HPMSAR will be increasingly used in future spaceborne SAR systems. This paper has reported the system design aspects for HPMSAR with an electronically steered antenna. A novel continuation-mode SAR acquisition has been introduced, which could simultaneously scan multidirectional subswaths without a shorter target illumination time than TOPS and ScanSAR. The system analysis to be considered in HPMSAR with an electronically steered antenna has been introduced and discussed, i.e., the system azimuth resolution, transmit beampattern design, TFD support, PRF selection. For the overlapped echoes and ambiguities, we have presented the 2-D DBF with multichannel unambiguous reconstruction technology, which is most likely to be the best choice for signal processing in future spaceborn HPMSAR. And the simulation results show the excellent system performance compared with conventional method. However, the results obtained for HPMSAR do not represent the full possible performance but give a good indication about the potentials and challenges for the operation of multichannel systems in HPMSAR system.

As a next step, based on the analysis of HPMSAR, focus should be on the adaptation of the system design to multichannel HPMSAR operation in combination with a further development of the HPMSAR multichannel processing. This includes orthogonal waveform design in transmit, system optimization for multichannel processing and different parameter selections. These features make HPMSAR the preferred candidate (assuming that antenna-steering technology and the available instrument technology are available) for ultra-resolution below 1m and ultrawide swaths of several hundred kilometers applications, whereas ScanSAR and TOPS

would still be much more useful for those applications where coarse geometric resolution, but simpler equipment, is needed. In conclusion, the results for this new system show that this new class of multichannel systems enables frequent mapping on a global scale with unprecedented detail. This means that such systems open up an entirely new field of SAR operation and introduce a new degree of freedom in SAR system design.

Acknowledgments

The authors would like to thank the editor and anonymous reviewers for their valuable time, comments, and suggestions to improve the quality and readability of this paper.

References

[1] G. Krieger, N. Gebert and A. Moreira, "Unambiguous SAR signal reconstruction from nonuniform displaced phase center sampling", IEEE Geosci. Remote Sens. Lett., vol. 1, no. 4, **(2004)**, pp. 260–264.
[2] N. Gebert, G. Krieger and A. Moreira, "Multichannel Azimuth Processing in ScanSAR and TOPS Mode Operation", IEEE Transactions on Geoscience and Remote Sensing, vol. 48, no. 7, **(2010)**, pp. 2994 - 3008.
[3] F. De Zan and A. M. Guarnieri, "TOPSAR: Terrain Observation by Progressive Scans", IEEE Transactions on Geoscience and Remote Sensing, vol. 44, no. 9, **(2006)**, pp. 2352-2360.
[4] C. Gao, R. Wang and Y. Deng, "Large-Scene Sliding Spotlight SAR Using Multiple Channels in Azimuth" , IEEE Geoscience and Remote Sensing Letters, vol. 10, no. 5, **(2013)**, pp. 1006-1010.
[5] D. Guo, H. Xu and J. Li, "Extended wavenumber domain algorithm for highly squinted sliding spotlight SAR data processing", Progress In Electromagnetics Research, vol. 114, **(2011)**, pp. 17–32.
[6] D. X. An, Z. M. Zhou, X. T. Huang and T. Jin, "A novel imaging approach for high resolution squinted spotlight SAR based on the deramping-based technique and azimuth NLCS principle", Progress In Electromagnetics Research, vol. 123, **(2012)**, pp. 485–508.
[7] A. Meta, J. Mittermayer and P. Prats, "TOPS Imaging With Te rraSAR-X: Mode Design and Performance Analysis", IEEE Transactions on Geoscience and Remote Sensing, vol. 48, no. 2, **(2010)**, pp. 759-769.
[8] J. Paul Browning, D. R. Fuhrmann and M. Rangaswamy, "A hybrid MIMO phased-array concept for arbitrary spatial beampattern synthesis", IEEE Digital Signal Processing and Signal Processing Education Workshop (DSP/SPE'09), Marco Island, FL, **(2005)**.
[9] A. Hassanien and S. A. Vorobyov, "Phased-MIMO Radar: A Tradeoff Between Phased-Array and MIMO Radars", IEEE Transactions on Signal Processing, vol.58, no.6, **(2010)**, pp. 1-33.
[10] D. R. Fuhrmann, J. P. Browning and M. Rangaswamy, "Signaling Strategies for the Hybrid MIMO Phased-Array Radar", IEEE Journal of Selected Topics in Signal Processing, vol. 4, no. 1, **(2010)**, pp. 66-78.
[11] G. Hua and S. S. Abeysekera, "Receiver Design for Range and Doppler Sidelobe Suppression Using MIMO and Phased-Array Radar", IEEE Transactions on Signal Processing, vol. 61, no. 6, **(2013)**, pp. 1315-1326.
[12] W. Q. Wang and H.Shao, "A Flexible Phased-MIMO Array Antenna with Transmit Beamforming", International Journal of Antennas and Propagation, **(2012)**, pp. 1-10.
[13] L. Zhang and D. Chen, "Digital Beamforming on Receive in Elevation for Spaceborne Hybrid Phased-MIMO SAR", Progress In Electromagnetics Research M, vol. 40, **(2014)**, pp. 153–166.
[14] G. Krieger, N. Gebert and A. Moreira, "Multidimensional Radar Waveforms", Geoscience and Remote Sensing Symposium, Barcelona, **(2007)**.
[15] G. Krieger, N. Gebert, M. Younis and A. Moreira, "Advanced Synthetic Aperture Radar Based on Digital Beamforming and Waveform Diversity", Radar Conference, Rome, **(2008)**.
[16] G. Krieger, N. Gebert and A. Moreira, "Multidimensional Waveform Encoding: A New Digital Beamforming Technique for Synthetic Aperture Radar Remote Sensing", IEEE Transactions on Geoscience and Remote Sensing, vol. 46, no. 1, **(2008)**, pp. 31-46.
[17] W. Q. Wang, "MIMO SAR OFDM Chirp Waveform Diversity Design With Random Matrix Modulation", IEEE Transactions on Geoscience and Remote Sensing, vol. 53, no. 3, **(2014)**, pp. 1-11.
[18] F. K. LI and W. T. K. JOHNSON, "Ambiguities in Spaceborne Synthetic Aperture Radar Systems", IEEE Transactions on aerospace and electronic system, vol. 19, no. 3, **(1983)**, pp. 389-397.
[19] M. Younis, S. Huber and A. Patyuchenko, "Performance Comparison of Reflector-and Planar-Antenna Based Digital Beam-Forming SAR", International Journal of Antennas and Propagation, **(2009)**, pp. 1-13.
[20] M. Villano, G. Krieger and A. Moreira, "Staggered SAR: High-Resolution Wide-Swath Imaging by Continuous PRI Variation", IEEE Transactions on Geoscience and Remote Sensing, vol. 52, no. 7, **(2014)**, pp. 4461-4479.

[21] G. Krieger, M. Younis, S. Huber and F. Bordoni, "Digital Beamforming and MIMO SAR: Review and New Concepts", EUSAR, **(2012)**.
[22] N. GEBERT, G. KRIEGER and A. MOREIR, "A Digital Beamforming on Receive: Techniques and Optimization Strategies for High-Resolution Wide-Swath SAR Imaging", IEEE Transactions on aerospace and electronic system, vol. 45, no. 2, **(2009)**, pp. 564-592.
[23] C. Y. Tseng, "Minimum Variance Beamforming with Phase-Independent Derivative Constraints", IEEE Transactions on antennas and propagation, vol. 40, no. 3, **(1992)**, pp. 285-294.
[24] B. D. Carlson, "Covariance Matrix Estimation Errors and Diagonal Loading in Adaptive Arrays", IEEE Transactions on aerospace and electronic systems, vol. 24, no. 4, **(1988)**, pp. 397-401.

